JOURNAL OF THERMOPHYSICS AND HEAT TRANSFER
Vol. 10, No. 2, April–June 1996

Examination of OH Ultraviolet Radiation from Shock-Heated Air

Deborah A. Levin*
Institute for Defense Analyses, Alexandria, Virginia 22311-1772
Robert J. Collins,† Graham V. Candler,‡ and Michael J. Wright§
University of Minnesota, Minneapolis, Minnesota 55455
and
P. W. Erdman¶
University of Pittsburgh, Pittsburgh, Pennsylvania 15260

Two recent sounding rocket experiments obtained spectral data at wavelengths of 200–400 nm from the shock-heated air surrounding a vehicle under flight conditions of 3.5 km/s at altitudes of 40–70 km and 5 km/s for altitudes of 110–65 km. Previous analyses of the data have emphasized modeling the radiation from the NO molecular system. The chemical kinetics of OH, a trace species in the flow, and the electronic state excitation mechanisms are simpler than those for NO. Hence, the comparison between modeling and data potentially provides a clearer assessment of the modeling of the flow thermochemical processes. This article discusses the OH flowfield and radiation models that we have developed, comparisons with data, and the implications of this work to ongoing NO flow and radiation modeling. Additional data from the side-viewing spectrometers from the 5-km/s flight will also be presented and analyzed. The angular dependence of the photometer data was compared with a solution obtained from a viscous three-dimensional flowfield calculation with reacting water chemistry.

Nomenclature

A = excited electronic state designation of OH, Einstein A coefficients or, predissociation rate, s^{-1}
f = temperature functional form
h = Planck's constant, 6.625×10^{-27} erg-s
k = reaction rate, cm^3/mole-s, cm^3/mol-s, Boltzmann's constant, 1.38×10^{-16} erg/K
M = third body neutral species such as N_2 or O_2
T = translational temperature, K
T_{rot} = rotational temperature, K
T_v = vibrational temperature, K
t = time, s
u = flow velocity, m/s
$\hat{u}$ = diffusion velocity, m/s
w = chemical source function, kg/m^3-s
X = ground electronic state designation of OH
x = flow direction, m
μ = reduced mass, amu
$\bar{\nu}$ = average collisional velocity, cm/s
ρ = mass density, kg/m^3
τ = OH(A) state lifetime, s
υ = frequency of light, Hz
υ' = initial vibrational state
υ'' = final vibrational state

Subscripts
d = predissociation
f = forward
j = flow direction
r = reverse
s = species index
0 = initial condition

Superscripts
ex = exchange
[ ] = concentrations

Presented as Paper 95-0708 at the AIAA 33rd Aerospace Sciences Meeting and Exhibit, Reno, NV, Jan. 9–12, 1995; received Sept. 14, 1995; revision received Nov. 27, 1995; accepted for publication Nov. 29, 1995.

*Research Staff Member, Science and Technology Division. Member AIAA.
†Professor Emeritus, Department of Electrical Engineering.
‡Associate Professor, Department of Aerospace Engineering and Mechanics. Member AIAA.
§Graduate Student, Department of Aerospace Engineering and Mechanics. Member AIAA.
¶Research Associate Professor, Department of Physics and Astronomy. Member AIAA.

Introduction

THE first bow shock flight experiment (April 1990) measured the ultraviolet (uv) radiation from shock-heated gas in the nose region of a 0.1016-m nose radius rocket traveling at 3.5 km/s at altitudes from 40 to 70 km (Ref. 1). The second bow shock flight experiment (February 1991) provided similar types of uv data during re-entry at 5 km/s between the altitudes of about 110–65 km for the flow passing over both the nose region and about 1 m further down the body.[2] The description of the instrumentation for these two flights that measured the OH radiation in the 310-nm spectral region has been described earlier.

The emphasis of the data analyses for the bow shock flights has been to understand the radiation emitted between 190–260 nm, because of the NO molecular system.[3,4] The altitude dependence of the ratio of the OH-to-NO radiation was analyzed through finite rate chemical kinetics, modeling at temperatures and densities typical of flow conditions for the first flight. However, none of the OH data has been analyzed with thermochemical–nonequilibrium flow and radiation models. With the interest in predicting the OH radiation at conditions different than the first two flights.[5] It is timely to develop a computa-

tional fluid dynamics (CFD) and radiation model that can be compared with data of 1-nm spectral resolution.

The study of the OH system is amenable to detailed flow and radiation modeling. The chemical kinetics analyses of the bow shock 1 conditions show that OH production occurs through a single-step process by the dissociation of trace amounts of water vapor present under ambient conditions. The formation of OH is more direct than the two-step process required to form NO. Therefore, there is less uncertainty in the reaction modeling, and it is possible to more easily evaluate the flow thermochemical models. The observed radiation at 310 nm is because of a transition from a single electronic excited state, in contrast to the uv emission from the NO molecule. The extensive laser-induced fluorescence database of cross sections for vibrational and rotational state-specific electronic quenching mechanisms improves the fidelity of the radiation calculations well beyond what is possible for NO.

The research presented in this article involved the development of 1) a simplified OH kinetics–radiation model; 2) a new CFD method that allows the inclusion of detailed mechanisms for the formation of trace species (such as OH or NO) for two- and three-dimensional flows; and 3) a multitemperature, spectral radiation model. The main results are summarized next.

The need to analyze the OH data at different viewing geometries and two flight conditions encouraged the development of a simplified kinetics–radiation model. The density dependence of the data was found to change from the first to the second flight. This combined model was useful in developing an excitation model to explain why the density dependence of the data varies from linear at high densities to cubic at low densities. The mechanisms found to be important were used in constructing the new CFD and radiation models that were applied to the forward- and side-viewing observations.

Since the altitude of the second flight was higher than the first, a new approach to the CFD modeling was found to be necessary. For the stagnation region, a multitemperature, reacting mixture of dry air gases was modeled. Since water and its chemical derivatives represent less than 1 part in 10^5 per volume, its presence does not change the bulk flow energy and momentum. Hence, the water thermochemistry model was incorporated in a simplified conservation law for the hydrogenated (trace) species. The important implications of this overlay implementation for reacting trace species is also discussed in this article.

To evaluate the data seen through the periscopes (of the second flight), a nonreacting, three-dimensional viscous calculation was undertaken to provide estimates of the gas translational temperature and total number densities. The overlay approach was then used to calculate the OH concentrations.

Finally, an absolute, spectral radiation model was developed for OH. In addition, major modifications were made to the computational technique used before. Previous work[6,7] assumed that the vibrational state distribution of excited electronic states is described by the ground-state bulk flow vibrational temperature. With a vibrational-state-specific treatment of the electronic excitation/de-excitation mechanisms, the vibrational temperature of the emitting species can be modeled and compared with spectral data. The vibrational temperature of OH will be shown to be very different from that of the major constituents in the flow. Hence, the common assumption that the vibrational temperature of other radiating molecular species formed in the shock layer is the same as that of N_2 is likely to be incorrect.

With this more complete set of modeling capabilities, important questions can be answered. This article discusses the source of the OH for the second flight, forward-viewing, high-altitude spectra and its relationship to the first flight. The OH vibrational temperature is derived from these spectra and compared with theory. Comparison of the absolute magnitudes of the computed and measured OH radiation was found to be consistent with atmospheric models for water. Finally, the utility of the side-viewing OH measurements, although complicated by vehicle motion effects, is shown to be useful for testing the fidelity of the three-dimensional calculations. The angular-functional agreement between the photometer data and calculations was found to be excellent.

Flight Data

Figure 1 shows a summary of the early re-entry scans observed in the forward-viewing spectrometer during the second bow shock flight experiment. Spectra were observed at lower altitudes, but as in the first flight,[1] the OH radiation is subsumed by the NO band systems. Spectral data from both flights show that the ratio of the predominant OH peak (310 nm) to the NO peaks (200–260 nm) increases with altitude. Figure 1 shows that at an altitude of about 100 km the OH radiation can still be observed with a magnitude of 3×10^{-8} W/cm^2 μ sr (an average over five scans). The lack of NO radiation at 100 km allows the OH(A, $v' = 1 \rightarrow X$, $v'' = 0$) peak at 280 nm to be observed. The presence of these two peaks permits us to evaluate the OH vibrational temperature.

In addition to the forward-viewing instruments, there were eight photometers and a scanning spectrometer (identical to the forward-viewing one) viewing the flow 1.25 m downstream of the vehicle nose and looking perpendicular to the nominal direction of flight. Figure 2 shows a simplified schematic of the two instrument viewing geometries and vehicle motion. Of these instruments the following three are of interest to the OH radiation analyses: 1) a photometer with center wavelength set at 310 ± 4 nm (the peak of an OH transition), 2) a photometer centered at 230 ± 25 (the NO gamma and beta-band systems), and 3) a scanning spectrometer (200–400 nm with 1-nm resolution). The intensity of the OH photometer as a function of time is shown in Fig. 3. It can be seen that the signal is modulated at the payload spin frequency with a period of approximately 0.47 s. During the portion of the flight for which data is shown in Fig. 3, the angle of attack of the payload was 10 deg, higher than anticipated. The large variation in intensity was caused by the coupling of the angle of attack with the spin motion, making the flow asymmetric. While this modulation hampered the reduction of the spectral data, the large modulation with angle permits a test for three-dimensional flow calculations.

Figure 4 shows an average of all side-viewing spectral scans taken as the spinning rocket descended from 72 to 65 km. This composite spectra shows the two major components of the OH molecular spectra, a peak at 310 and one at 280 nm and an additional structure. The separation of the OH spectra from the additional structure (most likely NO) was determined by look-

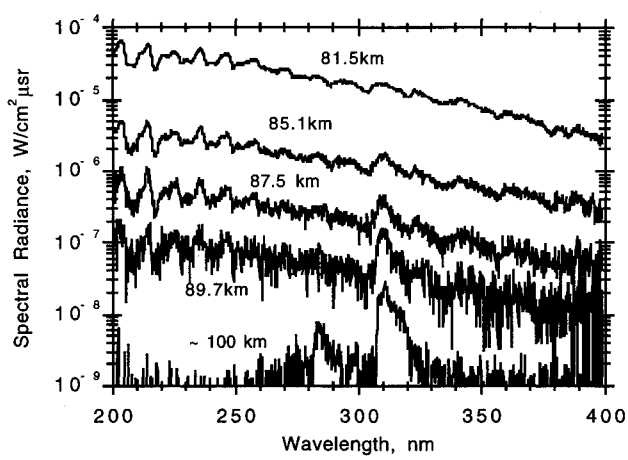

Fig. 1 Spectral scans from the forward-viewing spectrometer of ultraviolet bow shock radiation taken during re-entry of the second flight. The spectra shown at approximately 100 km is the average of scans taken over the altitude range of 110–95 km.

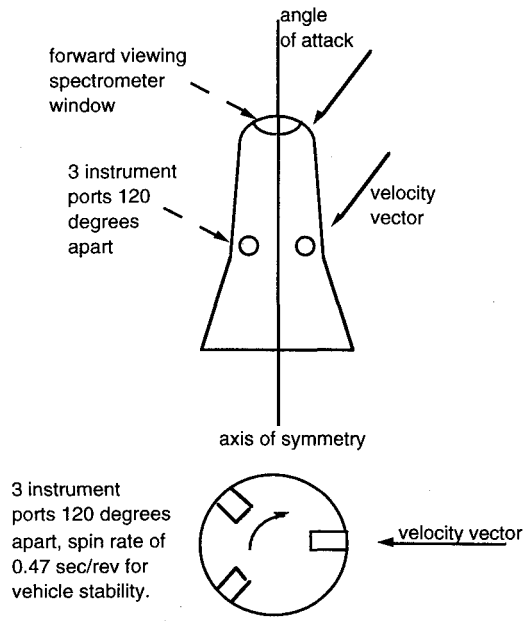

Fig. 2 Instrument viewing geometry for the precessing rocket motion (not drawn to scale).

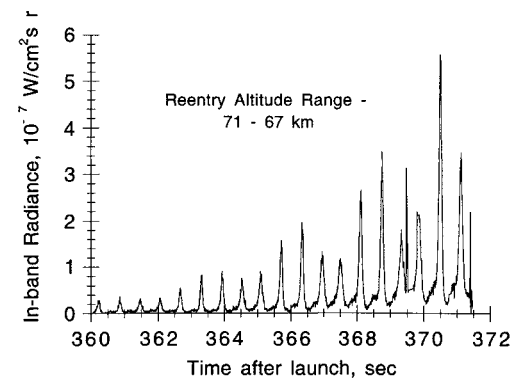

Fig. 3 Intensity of the OH 310 ± 4 nm side-viewing photometer as a function of time.

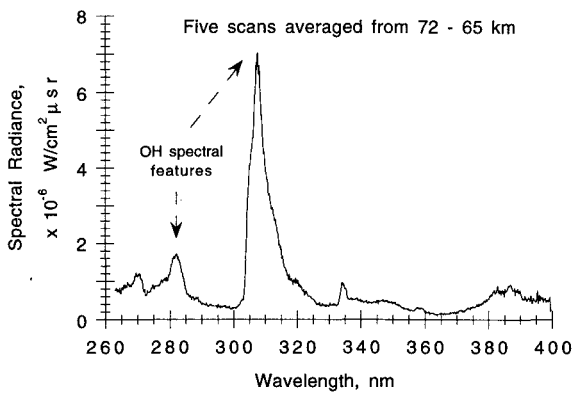

Fig. 4 Sum of all side-viewing spectral scans taken as the spinning rocket descends from 72 to 65 km.

ing at individual spectral scans of the digital data for the bialkali detector of the uv spectrometer. The spectrometer scans in wavelength in a continuous fashion from 400 to 250 nm and then from 250 to 400 nm. The time for this total scan is 1.95 s. Figure 2 shows that both the spectrometer and the photometer field of view (FOV) varied from the windward side to the leeside during each revolution of the rocket. The near-synchronous behavior of the scan and vehicle rotation rates implies that not all wavelengths will be observed while the spectrometer FOV is in the direction of maximum signal. When individual spectral scans are examined, this effect can be seen quite clearly; i.e., the spectral nature changes dramatically from scan to scan. It was happenstance that the scanning spectrometer was tuned to 310 nm when the rocket had rotated such that the normal component of the off-axis velocity vector coincided with the viewing axis. The composite spectra of Fig. 4 represents an average of spectral scans for different alignment conditions. However, it should be noted that the time to scan between 280–310 nm is less than the half width of the peak, as seen in the photometer data (Fig. 3).

References 1 and 2 discuss the calibration of the spectrometers and photometers. All instruments were calibrated with NIST-traceable sources and had absolute accuracy of about ±20%. The spectrometers and photometers were also cross calibrated.

Kinetic Analyses

To guide the flow, modeling a separate, kinetic analysis was undertaken using flow conditions representative of the bow shock ultraviolet (BSUV) 2 flight experiment. The modeling also permitted order of magnitude level comparison with the data. The set of reactions added to dry air chemistry were

$$O_2 + H \xleftrightarrow{k_1} O + OH \quad (1a)$$

$$H_2O + N_2 \xleftrightarrow{k_2} H + OH + N_2 \quad (1b)$$

$$OH + N \xleftrightarrow{k_3} NO + H \quad (1c)$$

$$H_2O + O \xleftrightarrow{k_4} OH + OH \quad (1d)$$

$$H + O + N_2 \xleftrightarrow{k_5} OH(A) + N_2 \quad (1e)$$

$$OH(A) + N_2 \xleftrightarrow{k_6} OH + N_2 \quad (1f)$$

$$OH(A) \xrightarrow{k_{7f}} OH + h\nu \quad (1g)$$

Table 1 gives the values for the rates in Eq. (1) (Refs. 8–11). To explore the BSUV 2 flight conditions, a matrix of temperatures from 2000 to 10,000 K and total molecular densities from 5×10^{12} to 1×10^{16} mol/cm^3 was used. For these cases the time-dependent concentration of OH, OH(A), and NO was determined using the Chemkin code.[12] For these exploratory calculations it was assumed that the ambient water mixing ratio per volume was 10^{-5}. This assumption will be discussed further later. Conditions typical of the second flight conditions at 90 km altitude and 5 km/s are a gas temperature of 10,000 K and a total number density of 1×10^{13}/cm^3. Comparison of the kinetic solution at these conditions with the solutions presented in Ref. 3 show that there is considerably less water dissociated than for the first flight conditions. From the matrix of conditions considered it was found that the second reaction dominates the production of OH. The collisionally induced excitation mechanism [reverse reaction of Eq.

Table 1 OH thermochemical kinetics model[a]

Reaction	C_{fi}[a]	η_i	E_{fi}/R[b]	Reference
1	2.2×10^{14}	0.0	16,646	8
2	3.5×10^{16}	0.0	100,510	8
3	4.0×10^{13}	0.0	0	8
4	6.8×10^{13}	0.0	9,240	8
5	1.2×10^{13}	0.0	6,940	9
6	9.8×10^{11}	0.5	0.0	10
7	1.4×10^{6}	0.0	0.0	11

[a]Rates are in cm^3/mole/s (or higher).
[b]R = 1.9872 cal/mole-K, E_{fi} is in cal/mole.

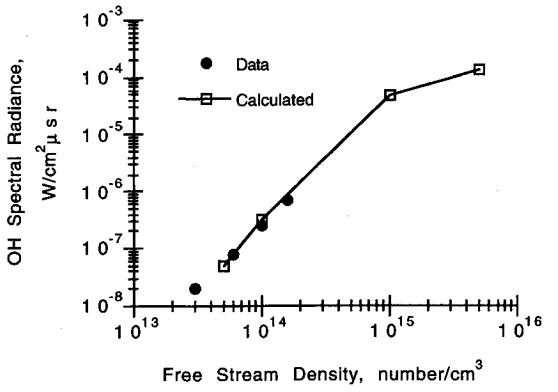

Fig. 5 Comparison of the BSUV 2 OH spectral peak heights with radiances calculated from OH concentrations derived from the kinetics analyses.

(1f)] was the only important mechanism in the production of OH(A). To use the kinetics model solutions, an estimate of the gas residence time in the FOV of the forward spectrometer was made. For these flow conditions it was found that a value of 100-μs residence time was reasonable and was used to compare the computed OH(A) concentration with the data.

Figure 5 shows the measured spectral peaks at 310 nm as a function of altitude or freestream density. The data were obtained from the forward-viewing spectrometer with the radiance contributions from other radiators (principally NO) at 310 nm subtracted. Also shown are the computed radiances using the OH(A) concentrations of the kinetics analyses. The calculated radiances assume an optical bandwidth of 0.008μ, a radiative lifetime of 700 ns, and an effective radiating length of 1 cm. Figure 5 shows that the density dependence of the data varies from cubic at low densities to linear at high densities.

The results of Fig. 5 may be explained with closed-form density-dependent expressions for the concentration of OH(A). For flow conditions at which all data were taken, the OH(A) lifetime τ is short compared to flow and reaction times. Hence, OH(A) will be in steady state with respect to its ground state:

$$[\mathrm{OH}(A)]/(\mathrm{OH}) = k_{6r}\mathrm{N}_2/(k_{6f}\mathrm{N}_2 + 1/\tau) \tag{2}$$

Equation (1b) is the dominant process for the formation of OH or

$$\frac{\mathrm{d(OH)}}{\mathrm{d}t} \approx k_{2f}(\mathrm{H_2O})(\mathrm{N_2}) - k_{2r}(\mathrm{OH})(\mathrm{H})(\mathrm{N_2}) \tag{3}$$

The two important limits of Eq. (3) are for times at and far from the steady state.

First consider the steady-state case. The number density of H, OH, and H_2O must be equal to the initial concentration of water, $(H_2O)_0$, and equal amounts of OH and H are produced. Setting Eq. (3) equal to zero and applying species conservation gives an expression for the concentration of OH:

$$(\mathrm{OH}) = \frac{-k_{2f} + \sqrt{k_{2f}^2 + k_{2f}k_{2r}(\mathrm{H_2O})_0}}{k_{2f}} \tag{4}$$

In the present case $k_{2f} > k_{2r}$ and $(H_2O)_0$ is also small (the fraction of water is one part in 10^{-5} or less). Using a binomial expansion for the square root term of Eq. (4) gives the simple result

$$(\mathrm{OH}) \cong \tfrac{1}{2}(\mathrm{H_2O})_0 \tag{5}$$

Equation (5) is only valid when the water has been largely decomposed. These conditions are encountered for temperatures on the order of 8000 K and pressures of 0.01 atm for the first bow shock flight. In the high-density and high-temperature limit, the collisional processes in Eq. (2) dominate. Substitution of Eq. (5) into Eq. (2) shows that the steady-state OH concentration is linear with density, as implied by Fig. 5.

Consider the other limit of Eqs. (2) and (3), i.e., the chemical kinetics are far from steady state and the collisional excitation rates are low. Initially Eq. (3) has the form

$$\frac{\mathrm{d(OH)}}{\mathrm{d}t} \approx k_{2f}(\mathrm{H_2O})(\mathrm{N_2}) \tag{6}$$

The [OH(A)]/(OH) ratio is still in steady state, but collision terms no longer dominate. Instead,

$$[\mathrm{OH}(A)]/(\mathrm{OH}) = k_{6r}(\mathrm{N_2})\tau \tag{7}$$

In this case the intensity does not vary linearly with density. Instead there is a density dependence for both the concentration of OH and the ratio of [OH(A)] to (OH). This leads to a cubic dependence at the lowest densities.

The density dependence of the data appears to be almost a square law, because the data span altitudes between the two limits discussed previously. The high-density limit was not measurable on the second flight, since the OH radiation becomes subsumed by that of NO. The conditions of the first flight come closer to this limit.

Flowfield Simulation—Overlay Method

The primary CFD method that is used to simulate the stagnation region for the cases of interest here is discussed in Refs. 4 and 13. A finite volume method is used to solve the Navier–Stokes equations, extended to account for finite rate chemical reactions and internal energy relaxation. The model for wet air is a reacting mixture of perfect gases composed of eight chemical species (N_2, O_2, NO, N, O, H_2O, H, and OH). The internal energy is described by translational, rotational, and vibrational–electron temperatures.

For the eight-species wet-air model, nine finite rate chemical reactions are considered:

$$\mathrm{N_2} + M \leftrightarrow \mathrm{N} + \mathrm{N} + M \tag{8a}$$

$$\mathrm{O_2} + M \leftrightarrow \mathrm{O} + \mathrm{O} + M \tag{8b}$$

$$\mathrm{NO} + M \leftrightarrow \mathrm{N} + \mathrm{O} + M \tag{8c}$$

$$\mathrm{N_2} + \mathrm{O} \leftrightarrow \mathrm{NO} + \mathrm{N} \tag{8d}$$

$$\mathrm{NO} + \mathrm{O} \leftrightarrow \mathrm{O_2} + \mathrm{N} \tag{8e}$$

$$\mathrm{O_2} + \mathrm{H} \overset{k_1}{\longleftrightarrow} \mathrm{O} + \mathrm{OH} \tag{8f}$$

$$\mathrm{H_2O} + \mathrm{N_2} \overset{k_2}{\longleftrightarrow} \mathrm{H} + \mathrm{OH} + \mathrm{N_2} \tag{8g}$$

$$\mathrm{OH} + \mathrm{N_2} \overset{k_3}{\longleftrightarrow} \mathrm{H} + \mathrm{O} + \mathrm{N_2} \tag{8h}$$

$$\mathrm{H_2O} + \mathrm{O} \overset{k_4}{\longleftrightarrow} 2\mathrm{OH} \tag{8i}$$

These chemical reactions are assumed to proceed in both the forward and reverse directions.

The dry air species forward rates are expressed in the standard Arrhenius form and correspond to those given in Table 2 of Ref. 3. The source of the Arrhenius parameters for the first five reactions and the computation of the reverse rates have been discussed in earlier work.[4,14] The ground-state reaction rates involving species with hydrogen were computed as follows. The forward rates were taken from the high-temperature data of Baulch.[8] The reverse rates were related to the forward rates with the assumption of detailed balancing. The equilibria constants were computed from the JANNAF database for high-temperature reactions.[12] The values of k_{1f} through k_{4f} used in

the flowfield simulations are those given in Table 1, except for Eq. (8h). The forward-rate constant coefficients used for k_{8f} were $C_{f3} = 7.5 \times 10^{14}$ cm^3/mole/s, $\eta_3 = 0.06$, and $E_{f3}/R =$ 100,470 cal/mole.

For conditions where the translational and vibrational temperatures are not equilibrated, it is common to assume that the dissociation reactions are governed by the geometric average of these two temperatures,[15] $\sqrt{TT_v}$. This model was developed to account for the reduction in the dissociation rate because of vibrational nonequilibrium. However, translational–vibrational relaxation for water is fast compared to that of N_2, so that other temperature weighting averages for the dissociation rates involving the hydrogenated species must be considered. The geometric weighting was retained for the forward dissociation rates of the dry air species.

Figures 6 and 7 show predicted stagnation streamline temperatures and species at 80 km and 5 km/s for a vehicle with a nose radius of 10.16 m. In the calculations the assumed mixing ratio of water in the freestream[16] was one part in 10^5. The high degree of thermochemical nonequilibrium is apparent from the temperature and species profiles. Comparison with chemical kinetic solutions obtained for the first bow shock flight experiment, at 3.5 km/s and 60 km altitude, shows that the degree of water dissociation is much less for the second flight conditions.[3]

Considering the flight data shown in Fig. 1, it can be seen that for the forward-viewing instruments the altitudes of interest for the second flight data are higher than 80 km. At these altitudes the use of full thermochemical models in the CFD calculations become more difficult because of long convergence times. Three additional species imply an even greater computational burden, particularly when many calculations are needed to test the sensitivities of various thermochemical modeling parameters.

Since water and its chemical derivatives are trace species, one would expect that the solution of their thermochemical properties could be decoupled from the full flow solution. Calculations made at 80 km with and without water gave identical temperatures and concentrations of all nonhydrogen-containing species. If the argument is made that the introduction of these trace species in the flow cannot affect the energy or momentum of the bulk solution, then a simplified conservation law for the expanded set of constituents (bulk + overlay or trace) can be written, which involves only the conservation of overlay species,

$$\frac{\partial \rho_s}{\partial t} + \frac{\partial(\rho_s u_j + \rho_s \hat{u}_{s,j})}{\partial x_j} = w_s \tag{9}$$

The velocity, temperatures, and nonoverlay species densities are held fixed during the overlay calculation. In this case, the bulk solution represents the CFD solution for dry air only. Hence, once the steady-state bulk solution has been obtained, Eq. (9) can be solved for different reaction sets, holding the bulk solution fixed. The solution of Eq. (9) is much less costly than the solution of the CFD for both bulk and overlay species because the cost varies approximately with the square of the number of equations being solved. Also, the overlay solution converges to a steady state quickly, and therefore, it is possible to incorporate detailed excited state chemistry models. Moreover, for altitude regimes where the continuum formulation becomes questionable, Eq. (9) can be solved using the bulk properties from the direct simulation Monte Carlo (DSMC) method.[17]

The overlay method provides a full spatial solution of the trace species concentrations. The ability to account for diffusion of light species through the flow, such as H, is particularly important for the modeling of the OH chemistry. Ignoring the diffusion effects produces spatial profiles significantly different (and incorrect) from those shown in Fig. 7. Hence, although the flow region of interest may be localized, a full spatial treatment is required.

A comparison of the species concentrations derived by the full CFD and this overlay method at 80 km showed complete agreement between the two methods. Figure 8 shows the hydrogenated species profiles obtained from the overlay method at an altitude of 88 km, where a full CFD calculation would be very expensive.

The three-dimensional flow computations to be compared with OH side-viewing data were performed as follows. The recently developed data-parallel LU relaxation method[18] was modified to solve the overlay conservation equations for the hydrogenated species, and excellent convergence properties were obtained.

Two three-dimensional flowfield simulations were performed for the BSUV 2 geometry at a 10-deg angle of attack at an altitude of 65 km. First, we used the DP-LUR method to solve the Navier–Stokes equations using a perfect gas equation of state. Then, the OH formation reaction set [Eqs. (8g–8i)] was overlaid on this flowfield. We used the perfect gas equation of state for the bulk solution because in the vicinity of the side-viewing photometer, the gas is relatively cold (peak temperature is 4118 K). Some vibrational energy excitation and oxy-

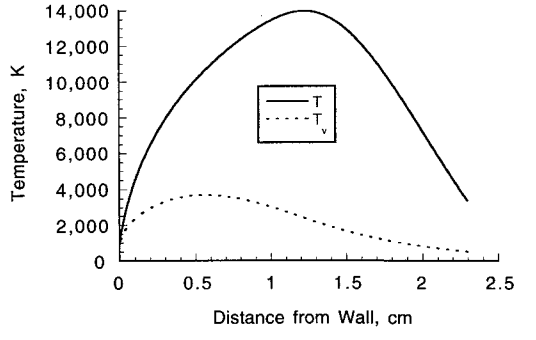

Fig. 6 Flow calculated temperatures at 80 km, 5 km/s, and a vehicle nose radius of 10.16 cm.

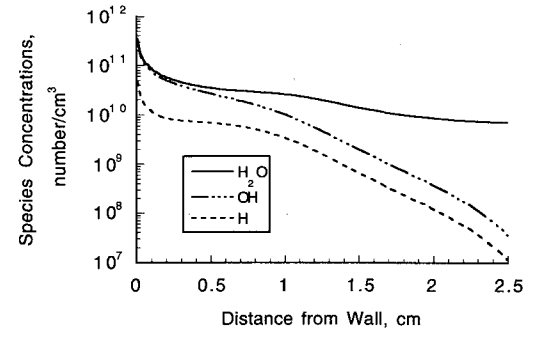

Fig. 7 Flow calculated hydrogenated species at 80 km, 5 km/s, and a vehicle nose radius of 10.16 cm.

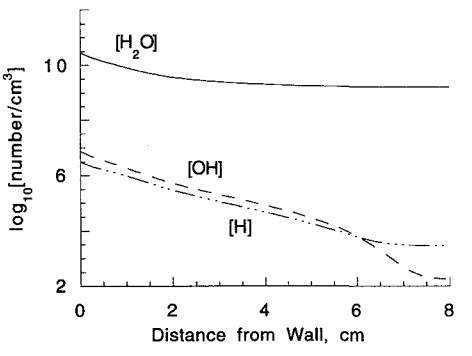

Fig. 8 Calculated overlay species at 88 km, 5 km/s, a vehicle nose radius of 10.16 cm, and a freestream water mixing ratio of 10^{-5}.

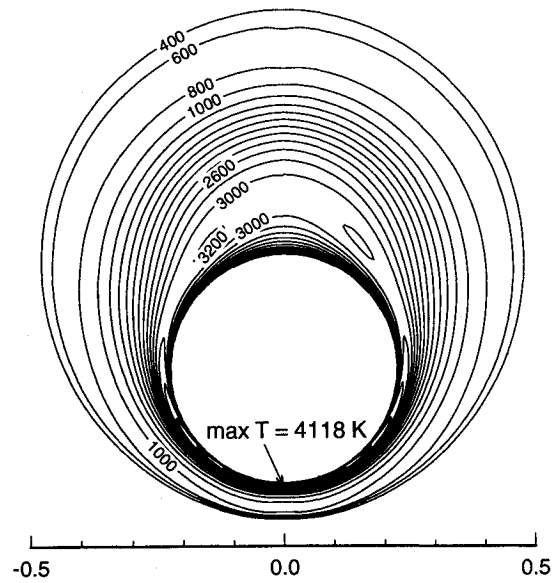

Fig. 9 Temperature contours in the plane of the BSUV 2 side-viewing windows at 65 km. The scale is meters.

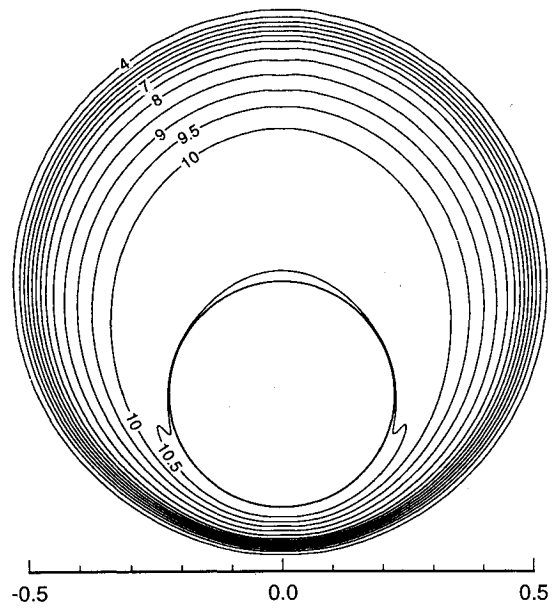

Fig. 10 OH concentration contours in the plane of the BSUV 2 side-viewing windows at 65 km. The scale is meters.

gen dissociation would occur at these conditions, but this would not change the results significantly. A grid with 128 points in the axial direction, 100 points in the normal direction, and 64 points in the circumferential direction was used. This grid was fitted to the body, and included the sphere–cone to a point just downstream of the viewing plane. Only one half of the body was simulated because of its bilateral symmetry. The computations were performed on a 64-node partition of the Army High Performance Computing Research Center CM-5.

Figures 9 and 10 are contour plots of gas temperature and the OH number density, respectively. As expected, there is a pronounced variation of the temperature and density with the angle from the windward side. The conditions shown in Figs. 9 and 10 will be used to model the side-viewing OH photometer data.

OH Radiation Model

The observed OH radiation (310 nm) is from the $A \rightarrow X$ transiation only. Hence, it can be modeled in greater detail and with higher confidence than the NO radiation between 190–300 nm, which involves transitions from four electronically excited states. There is also an extensive set of measurements that provides vibrational and rotational state-specific excitation cross sections for transitions among the X and A levels. Thus, it is possible to obtain state-specific expressions for the electronic state populations. Under the flight conditions the number of collisions is sufficiently high, so that the quasi-steady-state (QSS) assumption for electronic excitation is assumed to be valid.[7] The vibrational temperature of the A state can then be determined directly from the solution of the QSS equations. The usual assumption that the excited electronic state vibrational temperature is the same as that of the bulk flow species can thus be verified. Predissociation from the OH(A) state for vibrational levels greater than $v' = 2$ further reduces the manifold of vibrational states that need to be considered. The processes considered were

$$\begin{aligned} M + \mathrm{OH}(A, v' = 0) &\xrightarrow{k_{0x}} M + \mathrm{OH}(X) \\ M + \mathrm{OH}(A, v' = 1) &\xrightarrow{k_{1x}} M + \mathrm{OH}(X) \\ M + \mathrm{OH}(A, v' = 2) &\xrightarrow{k_{2x}} M + \mathrm{OH}(X) \end{aligned} \tag{10a}$$

$$\begin{aligned} \mathrm{OH}(A, v' = 2) &\xrightarrow{A_{2d}} \mathrm{O} + \mathrm{H} \\ \mathrm{OH}(A, v' = 3) &\xrightarrow{A_{3d}} \mathrm{O} + \mathrm{H} \end{aligned} \tag{10b}$$

$$\begin{aligned} \mathrm{OH}(A, v' = 0) &\xrightarrow{A_0} \mathrm{OH}(X) + h\nu \\ \mathrm{OH}(A, v' = 1) &\xrightarrow{A_1} \mathrm{OH}(X) + h\nu \\ \mathrm{OH}(A, v' = 2) &\xrightarrow{A_2} \mathrm{OH}(X) + h\nu \end{aligned} \tag{10c}$$

$$\begin{aligned} M + \mathrm{OH}(A, v' = 1) &\xrightarrow{k_{10}^{ex}} M + \mathrm{OH}(A, v = 0) \\ M + \mathrm{OH}(A, v' = 2) &\xrightarrow{k_{21}^{ex}} M + \mathrm{OH}(A, v = 1) \\ M + \mathrm{OH}(A, v' = 2) &\xrightarrow{k_{20}^{ex}} M + \mathrm{OH}(A, v = 0) \end{aligned} \tag{10d}$$

where M is a neutral third body. Equations (10a–10d) represent quenching, dissociation, spontaneous emission, and exchange processes, respectively. The reverse reactions for Eqs. (10a) and (10d) are also modeled.

The values for the rates used in the model are given in Table 2 (Refs. 10, 11, and 19). The measured cross sections are related to the rates by the average velocity:

$$\bar{v} = \sqrt{8kT/\pi\mu} \tag{11}$$

Table 2 OH vibrationally resolved excitation rates[a,b]

Rate	Units	Collision species	Source
$A_0 = 1.44 \times 10^6$	s^{-1}	——	Ref. 11
$A_1 = 0.36 \times 10^6$	s^{-1}	——	Ref. 11
$A_2 = 1.35 \times 10^6$	s^{-1}	——	Ref. 11
$k_{0x} = 3.7$ Å^2 $\bar{v}f(T)$	cm^3/mol-s	$M = N_2$	Ref. 10
$k_{0x} = 12$ Å^2 $\bar{v}f(T)$	cm^3/mol-s	$M = O_2$	Ref. 10
$k_{1x} = 4.9$ Å^2 $\bar{v}f(T)$	cm^3/mol-s	$M = N_2$	Ref. 19
$k_{1x} = 15.9$ Å^2 $\bar{v}f(T)$	cm^3/mol-s	$M = O_2$	Ref. 19
$k_{2x} = 0$	——	——	——
$A_{2d} = 3.7037 \times 10^6$	s^{-1}	——	Ref. 11
$A_{3d} = 1.0 \times 10^{10}$	s^{-1}	——	Ref. 11
$k_{10}^{ex} = 12$ Å^2 $\bar{v}$	cm^3/mol-s	$M = N_2$	Ref. 11
$k_{10}^{ex} = 2.1$ Å^2 $\bar{v}$	cm^3/mol-s	$M = O_2$	Ref. 11
$k_{21}^{ex} = 17.0$ Å^2 $\bar{v}$	cm^3/mol-s	$M = N_2$	Ref. 11
$k_{21}^{ex} = 2.0$ Å^2 $\bar{v}$	cm^3/mol-s	$M = O_2$	Ref. 11
$k_{20}^{ex} = 15.0$ Å^2 $\bar{v}$	cm^3/mol-s	$M = N_2$	Ref. 11
$k_{20}^{ex} = 0.5$ Å^2 $\bar{v}$	cm^3/mol-s	$M = O_2$	Ref. 11

[a]$T = 300$ K. [b]See text for definitions of $f(T)$ and $\bar{v}$.

The cross-sectional data have been obtained for a temperature of 300 K. The data of Fairchild et al.,[10] at 1100 K for the $A(v' = 0) \rightarrow X$ quenching, was used to determine a functional dependence for the rates [$f(T)$ of Table 3]:

$$f(T) = 0.375 \times \frac{\exp(687/kT)}{3.7}, \quad N_2 \qquad (12a)$$

$$f(T) = 10.6 \times \frac{\exp(450/kT)}{12}, \quad O_2 \qquad (12b)$$

The same reference suggests a value of $f(T)$ equal to unity for the vibronic energy exchange rates, k_{10}^{ex}, K_{21}^{ex}, and k_{20}^{ex}.

The NEQAIR (Ref. 6) model was generalized to solve for the QSS distribution of OH(A) in each of its three vibrational states. Following the computation of the distribution of vibronic states, the NEQAIR spectroscopic database was used to calculate the OH radiation. The spectroscopic data was improved to use more accurate vibrational–rotational energy terms[20] and the dependence of the line strength on rotational energy level.[21] Equations (10a–10d) imply a constant rotational dependence for the predissociation rates. An approximation used in this work was to assume predissociation from rotational states greater than 23, 12, and 4 for transitions from the $v' = 0$, 1, and 2 states, respectively.[20]

Comparison with Data

Consider again the forward-viewing spectra shown in Fig. 1. Comparison of these spectra with theory provides various types of basic modeling diagnostics: 1) predictability of the altitude dependence, 2) the validity of using the bulk temperatures to represent those of the OH(A) state, and 3) comments about the absolute magnitude of the calculated radiation. The results of these comparisons will be discussed in detail.

The freestream density dependence of the spectral peaks at about 310 nm provides information about the validity of the ground and excited state thermochemical models. Figure 11 shows a comparison of the spectral peak heights (data shown in Fig. 5) with our calculations of the OH(A) concentration integrated over the spectrometer FOV (the stagnation streamline). Data and calculations are plotted as a function of the freestream density normalized by the freestream density at 100 km. The calculated OH(A) concentration is the sum of the steady-state OH(A, v') concentrations summed over the three vibrational states. Two different ground-state thermochemical models were used in the calculation of the forward rates, k_{1f} through k_{4f}, of Eq. (8). These results are shown in the figure as the $(TT_{vib})^{1/2}$ model[15] and the T model.[17] It can be seen that the model that uses the translational temperature gives better density-dependent agreement with the data.

Figure 12 shows a comparison of the forward-viewing spectra obtained at the highest altitude, ~100 km, and a spectra

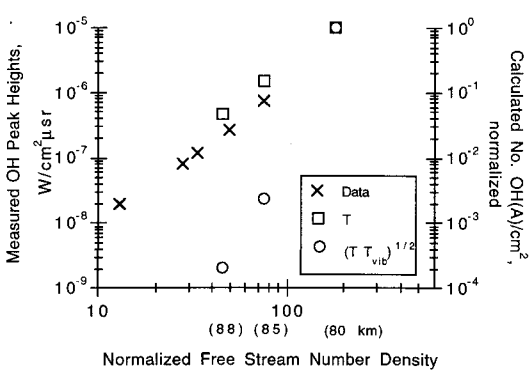

Fig. 11 Comparison of the forward-viewing OH spectral data and the overlay/OH(A) steady-state calculations for the BSUV 2 high-altitude conditions. The correspondence between the abscissa and altitude is indicated by the values in parentheses.

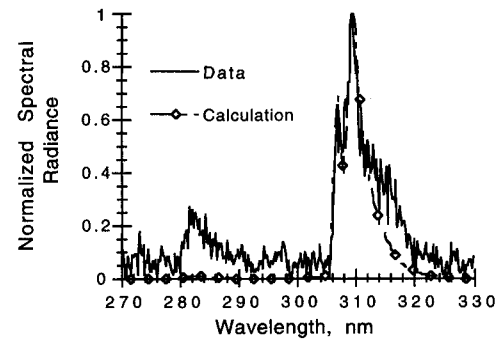

Fig. 12 Comparison of the forward-viewing normalized OH spectra at 100 km and the calculated spectra for the BSUV 2 high altitude conditions (88 km).

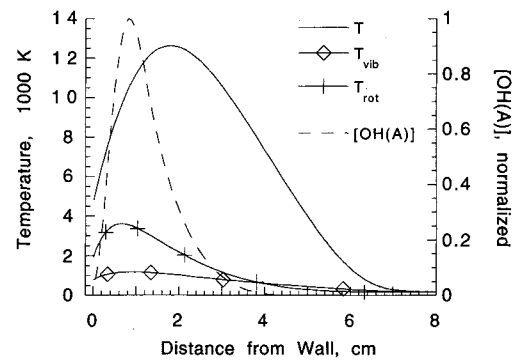

Fig. 13 Flow temperatures and excited state species stagnation streamline profiles at 88 km for the BSUV 2 flight conditions.

calculated at 88 km, each self-normalized. The rotational splitting of the OH(A, $v' = 0$) → OH(X, $v'' = 0$) structure near 310 nm is a good measure of the rotational temperature. The ratio of the peak heights at 280 ($v' = 1 \rightarrow v'' = 0$) and 310 nm and the shape of the right shoulder of the 310-nm peak structure depend on the vibrational temperature. Spectra were calculated (independent of the flow solution) for a matrix of rotational and vibrational temperatures between 2000–7000 K. This analysis showed that the experimental spectra could be best characterized by a rotational temperature between 2000–4000 K and a vibrational temperature between 5000–7000 K. Comparison of the spectra generated and measured shows that some, but not all, elements are in agreement. It appears that the rotational temperature of the bulk gas is in good agreement with the data. The lack of structure at 280 nm and the reduced shoulder of the 310-nm peak predicted by the flow and radiation modeling indicates that the bulk vibrational temperature is very different from the data. Figure 13 helps to elucidate this result. The bulk flow translational, vibrational, and rotational functions and the normalized OH(A) concentration are plotted as a function of distance from the wall along the stagnation streamline, or equivalently the FOV of the spectrometer. The measured spectra is dominated by those temperatures where the OH(A) concentration peaks. At that point in the flow the rotational temperature is seen to be about 3000 K, which is consistent with the temperature obtained from the spectral fit. The bulk vibrational temperature of 1000 K, however, is clearly much lower than that given by the spectral data.

Spectral fits were also obtained for the other BSUV 1 and 2 data shown in Fig. 1 and Ref. 1. The spectral fit at the highest altitude was considered to be the most reliable since no NO molecular background subtraction was required. Nevertheless, a vibrational temperature of about 5000 K was obtained for the other cases as well. Again, the vibrational temperature that best fit the data was found to be higher than that of the bulk gas.

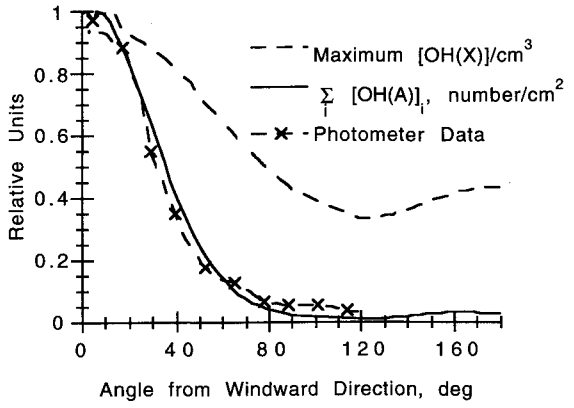

Fig. 14 Comparison of OH side-viewing photometer data and calculated OH and summed-OH(*A*) radiation angular dependence.

The calculated spectra shown in Fig. 12 has a peak absolute magnitude of 4.8×10^{-5} W/cm^2 μ sr, which can be compared with the magnitude of the spectra shown in Fig. 1 of about 2×10^{-7}. The most likely causes for this discrepancy can be attributed to errors in the modeling of the bulk flow translation temperature, the OH thermochemical model, or the freestream water mixing ratio. Detailed comparison of DSMC and CFD calculations for the bulk flow properties at the same 88-km conditions show good agreement in the bulk heavy particle translational temperature. The OH thermochemical model is fairly straightforward. In this calculation it was assumed that the forward dissociation rates were governed by the translational temperature. The absolute spectral magnitude (but not shape) was found to be very sensitive to different temperature weightings for the forward dissociation rates. Consistent with the chemical kinetics of OH formation, the magnitude increased for higher heavy particle translational temperature weighting. However, as shown in Fig. 11, the T weighting gives an altitude dependence consistent with the data.

As mentioned earlier, the freestream water mixing ratio was assumed to be 10^{-5} parts per volume. At a given altitude, the absolute magnitude of the OH radiation is linearly proportional to the freestream water concentration, because the forward process [Eq. (8g)] dominates. Hence, if the assumed freestream water concentration is too high, then the absolute magnitude could be reduced accordingly. The atmospheric data and models shows more variability in the data for the altitude range of the second flight than of the first. Above 90 km, the water mixing ratio could vary from 10^{-7} to 10^{-5} parts per volume.[16,22] Hence, the calculated absolute value can be shown to be within a factor of 2 of experiment. Alternatively, the modeling used in conjunction with the flight data can be viewed as providing an independent assessment of the concentrations of an atmospheric trace species.

The discussion in this section has emphasized what can be learned from the comparison of the calculations with the forward-viewing spectrometer. Now we compare the data obtained from the side-looking instruments with a three-dimensional flow simulation. The observed spectra averaged over scans taken as the rocket descended from 70 to 65 km (Fig. 4) suggests that OH radiation is the dominant feature in the side-looking spectra. The ratio of the two peaks should have given the vibrational temperature. The modulation imposed by the rotation and nearly harmonic relation between the scan rate and the rotation rate makes the assessment of the vibrational temperature more difficult than the forward-viewing data. At best, the ratio can be said to be consistent with a vibrational temperature between 3000–4000 K. Figure 9 shows that this temperature is in general agreement with the temperatures obtained from the viscous nonreacting three-dimensional flow calculations.

The three-dimensional flow temperatures, total number densities, and OH concentrations were used in the radiation model to calculate the OH(A) concentration at each flow grid point. Each radial corresponds approximately to the line-of-sight of the OH photometer, which varies as a function of angle from the windward direction. To compare with broadband photometric data, it is sufficient to sum the OH(A) concentration along each radial. Figure 14 shows a comparison of data and the calculated maximum-OH concentration, and, summed-OH(A) concentration as a function of angle. The agreement between the half-power point of the data and the calculated summed-OH(A) concentration is excellent for these nonsymmetric flow conditions. It can also be seen that the OH concentration at the location of the maximum temperature, along a given radial, has a much broader angular dependence than the data. This is because of the lack of coincidence of the maximum temperature and maximum OH concentration.

Conclusions

A number of important observations can be made from the research discussed in this article. There is sufficient water in the freestream to account for the radiation from OH that was observed in the bow shock 2 flight re-entry. Thus, the cause of the altitude dependence of the ratio of the OH/NO radiation observed in the second flight is similar to that observed in the first. A kinetic analysis demonstrated the key mechanisms for the production of OH in the ground and excited states. For the matrix of conditions considered, it was found that the collisionally induced dissociation of water dominates the production of OH. The neutral species collisionally induced excitation mechanisms was the only important term in the production of OH(A). These two conclusions are similar to our findings for the first flight conditions, but for the second flight conditions, there was considerably less water dissociation.

Two new computational models were developed. A computational flow method was shown to be able to efficiently model the chemical kinetics of trace species in a chemically reacting flow. The solution of the bulk or main flow species is held constant to permit detailed modeling of the trace species. The technique was successfully applied to the stagnation and aft regions of the vehicle. The species concentrations obtained from the overlay flow calculations were then used in the new OH radiation model.

Examination of the forward-viewing spectral data gave a number of significant results. It was found that for the second flight, high-altitude conditions, the vibrational temperature of the OH (A) system is different than that of the bulk flow. This may have implications for the modeling of uv emission in similar flows from other simple diatomic species. Comparison of the spectral radiance data with calculations showed that the heavy particle translational temperature characterized the water dissociation. The absolute magnitude of the computed spectra at 88 km suggests ambient water concentrations on the order of 10^{-7} parts per volume.

The modulations observed in the side-viewing spectroscopic and photometric data are caused by the nonzero angle of attack and the coning motion of the vehicle during re-entry. They have the undesirable effect of complicating the analysis of the data and reducing the amount of useful data. Nevertheless, sets of useful data were found and studied. It was found that the calculation closely reproduced the angular modulation observed in the photometric data.

Acknowledgments

This research was supported by the Innovative Science and Technology Directorate of the Ballistic Missile Defense Organization (BMDO), and directed by the Army Research Office. Research performed at the Institute for Defense Analyses was carried out under Contract DASW01-94-C-0054 for BMDO.

References

[1]Erdman, P. W., Zipf, E. C., Espy, P., Howlett, L. C., Levin, D. A., Loda, R., Collins, R. J., and Candler, G. V., "Flight Measurements of Low-Velocity Bow Shock Ultraviolet Radiation," *Journal of Thermophysics and Heat Transfer*, Vol. 7, No. 1, 1993, pp. 37–41.

[2]Erdman, P. W., Zipf, E. C., Espy, P., Howlett, L. C., Levin, D. A., Collins, R. J., and Candler, G. V., "Measurements of Ultraviolet Radiation from a 5-km/s Bow Shock," *Journal of Thermophysics and Heat Transfer*, Vol. 8, No. 3, 1994, pp. 441–446.

[3]Levin, D. A., Candler, G. V., Collins, R. J., Erdman, P. W., Zipf, E., Espy, P., and Howlett, C., "Comparison of Theory with Experiment for the Bow Shock Ultraviolet Rocket Flight," *Journal of Thermophysics and Heat Transfer*, Vol. 7, No. 1, 1993, pp. 30–36.

[4]Levin, D. A., Candler, G. V., Collins, R. J., Erdman, P. W., Zipf, E. C., and Howlett, L. C., "Examination of Theory for Bow Shock Ultraviolet Rocket Experiments—I," *Journal of Thermophysics and Heat Transfer*, Vol. 8, No. 3, 1994, pp. 447–452.

[5]Levin, D., Finke, R., Candler, G. V., Boyd, I., Howlett, L. C., and Erdman, P. W., "In-Situ Measurements of Transitional and Continuum Flow UV Radiation from Small Satellite Platforms," AIAA Paper 94-0248, Jan. 1994.

[6]Park, C., "Calculation of Nonequilibrium Radiation in the Flight Regimes of Aero-Assisted Orbital Transfer Vehicles," *Thermal Design of Aero-Assisted Orbital Transfer Vehicles*, edited by H. F. Nelson, Vol. 96, Progress in Astronautics and Aeronautics, AIAA, New York, 1985.

[7]Levin, D. A., Braunstein, M., Candler, G. V., Collins, R. J., and Smith, G. P., "Examination of Theory for Bow Shock Ultraviolet Rocket Experiments—II," *Journal of Thermophysics and Heat Transfer*, Vol. 8, No. 3, 1994, pp. 453–459.

[8]Baulch, D. L., Drysdale, D. D., Home, D. G., and Lloyd, A. C., "Evaluated Kinetic Data for High Temperature Reactions," *Homogeneous Gas Phase Reactions of the H_2-O_2 System*, Vol. 1, ISBN 0 408 70346 6, Butterworths, London, 1972.

[9]Hidaka, Y., Takahashi, S., Kawano, H., Sua, M., and Gardiner, W. C., "Shock-Tube Measurements of the Rate Constant for Excited OH($A\ ^2\Sigma^+$) Formation in the Hydrogen-Oxygen Reaction," *Journal of Physical Chemistry*, Vol. 86, 1982, pp. 1429–1433.

[10]Fairchild, P. W., Smith, G. P., and Crosley, D. R., "Collisional Quenching of $A^2\Sigma^+$ OH at elevated temperatures," *Journal of Chemical Physics*, Vol. 70, No. 4, 1983, pp. 1795–1807.

[11]German, K. R., "Radiative and Predissociative Lifetimes of the $v' = 0, 1, 2$ levels of the $A^2\Sigma^+$ state of OH and OD," *Journal of Chemical Physics*, Vol. 63, No. 12, 1975, pp. 5252–5255.

[12]Kee, R. J., Miller, J. A., and Jefferson, T. H., "CHEMKIN: A General-Purpose, Problem-Independent, Transportable, FORTRAN Chemical Kinetics Code Package," Sandia Rept. SAND80-8003 · UC-4, 1988.

[13]Candler, G. V., and MacCormack, R. W., "The Computation of Hypersonic Ionized Flows in Chemical and Thermal Nonequilibrium," *Journal of Thermophysics and Heat Transfer*, Vol. 5, No. 3, 1991, pp. 266–273.

[14]Park, C., "On Convergence of Computation of Chemically Reacting Flows," AIAA Paper 85-0247, Jan. 1985.

[15]Park, C., "Assessment of Two-Temperature Kinetic Model for Ionizing Air," AIAA Paper 87-1574, June 1987.

[16]*Handbook of Geophysics and the Space Environment*, edited by A. S. Jursa, U.S. Air Force Systems Command, Air Force Geophysics Lab., 1985.

[17]Boyd, I. D., Candler, G. V., and Levin, D. A., "Dissociation Modeling in Low Density Hypersonic Flows of Air," *Physics of Fluids*, Vol. 7, No. 7, 1995, pp. 1757–1763.

[18]Candler, G. V., Wright, M. J., and McDonald, J. D., "A Data Parallel LU Relaxation Method for Reacting Flows," *AIAA Journal*, Vol. 32, No. 12, 1994, pp. 2380–2386.

[19]German, K. R., "Collision and Quenching Cross Sections in the $A^2\Sigma^+$ State of OH and OD," *Journal of Chemical Physics*, Vol. 64, No. 10, 1976, pp. 4065–4068.

[20]Levin, D. A., Laux, C. O., and Kruger, C. H., "A General Model for the Spectral Calculation of OH Radiation in the Ultraviolet," AIAA Paper 95-1990, June 1995.

[21]Crosley, D. R., and Chidsey, I. L., "Tables of Calculated Transition Probabilities for the *A-X* System of OH," Ballistic Research Lab., ARBRL-TR-02326, Aberdeen Proving Ground, MD, 1981.

[22]Brasseur, G., and Solomon, S., *Aeronomy of the Middle Atmosphere*, Reidel Publishers, Dordrecht, The Netherlands, 1984.